3D Wave-Equation-Based Finite-Frequency Tomography for Ultrasound Computed Tomography

Naiara Korta Martiartu, Christian Boehm, and Andreas Fichtner

Abstract—Ultrasound Computed Tomography (USCT) has great potential for 3D quantitative imaging of acoustic breast tissue properties. Typical devices include high-frequency transducers, which makes tomography techniques based on numerical wave propagation simulations computationally challenging, especially in 3D. Therefore, despite the finite-frequency nature of ultrasonic waves, ray-theoretical approaches to transmission tomography are still widely used. This work introduces finite-frequency traveltime tomography to medical ultrasound. In addition to being computationally tractable for 3D imaging at high frequencies, the method has two main advantages: (1) It correctly accounts for the frequency dependence and volumetric sensitivity of traveltime measurements, which are related to off-ray-path scattering and diffraction. (2) It naturally enables out-of-plane imaging and the construction of 3D images from 2D slice-by-slice acquisition systems. Our method rests on the availability of calibration data in water, used to linearize the forward problem and to provide analytical expressions of cross-correlation traveltime sensitivity. As a consequence of the finite frequency content, sensitivity is distributed in multiple Fresnel volumes, thereby providing out-of-plane sensitivity. To improve computational efficiency, we develop a memory-efficient implementation by encoding the Jacobian operator with a 1D parameterization, which allows us to extend the method to large-scale domains. We validate our tomographic approach using lab measurements collected with a 2D setup of transducers and using a cylindrically symmetric phantom. We then demonstrate its applicability for 3D reconstructions by simulating a slice-by-slice acquisition system using the same dataset.

Index Terms—Ultrasound computed tomography (USCT), finite-frequency tomography, Born approximation, adjoint technique, breast imaging, resolution analysis, point-spread function, traveltime

I. INTRODUCTION

Ultrasound computed tomography (USCT) is an emerging technique for diagnostic imaging of breast tissue. In contrast to the commonly used sonography, USCT uses both transmission and reflection data to provide quantitative images of acoustic tissue properties. Empirical studies have demonstrated the diagnostic value of this information, enabling non-invasive tissue characterization and improving the specificity of standard imaging modalities [1]–[3].

Speed of sound, or velocity, is the most studied transmission property due to its strong correlation with tissue density [4], [5], a risk factor for breast cancer [6]. Typical USCT systems use ray-based tomographic algorithms to reconstruct this information from the first-arrival times [7]–[9]. These methods are robust and computationally efficient, making them very attractive for clinical practice. However, being based on

All the authors are with the Department of Earth Sciences, ETH Zurich, Zurich CH-8092, Switzerland e-mail: (naiara.korta@posteo.net).

the infinite-frequency assumptions, they neglect two essential aspects of the traveltime measurements: (1) In practice, traveltime differences are estimated by cross-correlating observed signals and calibration data within a limited frequency band. Therefore, the measurements are inherently frequency-dependent [10], meaning that results depend on the frequency content of the cross-correlated pulses. (2) Due to scattering and diffraction, the traveltimes of the finite-frequency waves are sensitive to tissue structure off the ray path. Consequently, the approximations of ray theory are only valid for media with heterogeneities larger than the wavelength and the first Fresnel volume [11].

To improve the spatial resolution of the reconstructions, significant efforts have been made to introduce imaging techniques that rely on more accurate descriptions of wave propagation [12]–[15]. This has led researchers to recognize similarities with seismology, and as a result, seismic waveform tomography has been transferred to USCT [16]–[19]. Waveform tomography accounts for all wave phenomena by numerically solving the wave equation. With sufficient data coverage and quality, it can provide images with subwavelength spatial resolution, however, at increased computational cost. Applications to *in vivo* data using slice-by-slice scanning systems have shown very promising results [16], [20]. These studies use 2D approximations of the wave equation to provide computationally tractable solutions. Therefore, artifacts may appear in the images due to out-of-plane scattering and diffraction [21]–[24]. The practical adaptation of 3D waveform tomography in medical ultrasound imaging still remains a challenge, mostly due to the high-frequency transducers used in the acquisition systems. The number of wavelengths propagated through the tissue exceeds 100 [25], which makes waveform tomography both computationally very expensive and highly sensitive to cycle-skipping and local minima [26], [27].

In this work, we present a novel approach to USCT that is computationally tractable for 3D imaging at high frequencies and still capable of accounting for first-order scattering and diffraction effects. This naturally enables out-of-plane imaging, which makes it well suited, for instance, for the construction of 3D images based on 2D slice-by-slice acquisition systems. Originally proposed in seismology [28]–[31], numerous studies have shown successful applications of finite-frequency tomography at regional [32]–[34] and global scales [35], [36]. The method is valid for velocity contrasts of up to 10% with respect to a background model [37], a condition that is guaranteed in breast tissue. Furthermore, finite-frequency considerations allow us to image velocity anomalies significantly smaller than the first Fresnel zone [38], [39]. This is especially true in the presence of adequate data

coverage, which can potentially be satisfied in USCT with rotations and translations of the acquisition system. Our work therefore brings the method to the context of USCT and honors the recent efforts for interdisciplinary collaboration between seismology and USCT.

The tomographic method we present is based on the Born approximation of the wave equation, and it uses adjoint techniques [40]–[43] to compute the Jacobian operator. The latter relates velocity perturbations to traveltime observations that are measured by the cross-correlation of ultrasonic signals with calibration data in water. This results in a large-scale linear inverse problem. We propose a cost-efficient implementation involving emitter-receiver geometry independent one-dimensional parameterizations of the sensitivity kernels, which allows massively parallelized operations on GPU architectures.

In what follows, we first introduce the theoretical aspects of the finite-frequency tomography method, and we propose practical implementations in the context of USCT. We then demonstrate its practical applicability using lab data for both 2D and 3D reconstructions. Finally, we discuss the resolution limits of the method, by relating it to the design of the acquisition systems.

II. FINITE-FREQUENCY TRAVELTIME TOMOGRAPHY

In USCT, we estimate the acoustic properties of breast tissue $\mathbf{m}$ from the observations of the space- and time-dependent pressure wavefield $p(\mathbf{x}, t)$ at transducer locations surrounding the breast. Observables and unknown parameters are related through the acoustic wave equation, which is formulated, in the time domain and for loss-less media, as

$$\frac{1}{c^2(\mathbf{x})}\partial_t^2 p(\mathbf{x}, t) - \rho(\mathbf{x})\nabla \cdot \left(\frac{1}{\rho(\mathbf{x})}\nabla p(\mathbf{x}, t)\right) = f(\mathbf{x}, t). \quad (1)$$

Here, $f(\mathbf{x}, t)$ is the source term, and the properties of the tissue are parameterized in terms of the velocity $c(\mathbf{x})$ and density $\rho(\mathbf{x})$, being $\mathbf{m} = [c(\mathbf{x}); \rho(\mathbf{x})]$. We denote by $p(\mathbf{x}_r, t; \mathbf{x}_s)$ the pressure field generated by an emitter at $\mathbf{x}_s$ and recorded at receivers $\mathbf{x}_r$, and in general, we take specific parts from this time series to define the observables.

Typically, density is assumed to be constant, and the velocity information is retrieved from the first-arrival traveltimes. This can be formulated as a least-squares problem, minimizing the sum of the squared residuals $\Delta T(\mathbf{x}_r, \mathbf{x}_s; \mathbf{m}) = T_{\mathrm{obs}}(\mathbf{x}_r, \mathbf{x}_s) - T(\mathbf{x}_r, \mathbf{x}_s; \mathbf{m})$ between the observed and predicted traveltimes for each emitter-receiver combination, respectively. In practice, first-arrival times are measured by the cross-correlation of the observed signals and calibration data. An internally consistent way of formulating the optimization problem is therefore by defining $\Delta T(\mathbf{x}_r, \mathbf{x}_s; \mathbf{m})$ as the time shift τ where the cross-correlation

$$C(\tau) = \int_{t_0}^{t_1} p_{\mathrm{obs}}(\mathbf{x}_r, t + \tau; \mathbf{x}_s)p(\mathbf{x}_r, t; \mathbf{x}_s, \mathbf{m})dt \quad (2)$$

attains its maximum. Here, $[t_0, t_1]$ is the time interval in which the first arrivals occur, and p_{obs} and p are the observed and modelled ultrasonic signals, respectively. In our derivations,

we closely follow [28]. If we drop the dependencies in $\mathbf{x}_r$ and $\mathbf{x}_s$ for clarity, ΔT satisfies

$$\left.\frac{dC(\tau)}{d\tau}\right|_{\tau=\Delta T} = \int_{t_0}^{t_1} \partial_t p_{\mathrm{obs}}(t + \Delta T)p(t; \mathbf{m})dt = 0. \quad (3)$$

This equation establishes the implicit relation between ΔT and $p(t; \mathbf{m})$. For simplicity, we denote $\partial_t p_{\mathrm{obs}}(t + \tau)|_{\tau=\Delta T} = \partial_t p_{\mathrm{obs}}(t + \Delta T)$. In particular, for the velocity estimations, we are interested in the relationship between the traveltime perturbations δT and velocity perturbations δc. From (3), by applying the chain rule for implicit differentiation and integration by parts, we obtain

$$\delta T = \frac{1}{N}\int_{t_0}^{t_1} \partial_t p_{\mathrm{obs}}(t + \Delta T)\frac{\partial p(t; \mathbf{m})}{\partial c}\delta c \, dt, \quad (4)$$

where

$$N = \int_{t_0}^{t_1} \partial_t p_{\mathrm{obs}}(t + \Delta T)\partial_t p(t; \mathbf{m})dt. \quad (5)$$

The derivatives of the wavefield with respect to the model parameters that appear in (4) can be computed from the Born approximation of (1). Assume we apply a perturbation in velocity $c \to c + \delta c$ that causes a first-order perturbation in the wavefield $p \to p + \delta p$. Then, the perturbed wavefield $\delta p = \frac{\partial p}{\partial c}\delta c$ is expressed, in terms of the Green's function G, as (e.g., [44])

$$\delta p(\mathbf{x}, t) = \int_V \int_{t_0}^{t_1} \frac{2\delta c}{c^3(\mathbf{x}')}\partial_t^2 p(\mathbf{x}', t')G(\mathbf{x}, t; \mathbf{x}', t')dt' \, d\mathbf{x}', \quad (6)$$

where V is the volume of our region of interest (ROI). By replacing (6) in (4), using the reciprocity of the Green's function

$$G(\mathbf{x}, t; \mathbf{x}', t') = G(\mathbf{x}', -t'; \mathbf{x}, -t), \quad (7)$$

and expressing the wavefield at $\mathbf{x}_r$ as

$$p(\mathbf{x}_r, t) = \int_V p(\mathbf{x}, t)\delta(\mathbf{x} - \mathbf{x}_r)d\mathbf{x}, \quad (8)$$

we obtain

$$\delta T(\mathbf{x}_r, \mathbf{x}_s) = \int_V K(\mathbf{x}; \mathbf{x}_r, \mathbf{x}_s)\delta c(\mathbf{x}) \, d\mathbf{x}. \quad (9)$$

Here, $K(\mathbf{x}) = K(\mathbf{x}; \mathbf{x}_r, \mathbf{x}_s)$ is the cross-correlation traveltime misfit sensitivity kernel defined as

$$K(\mathbf{x}) = \frac{-2}{c^3(\mathbf{x})}\int_{t_0}^{t_1} \partial_t p(\mathbf{x}, t; \mathbf{x}_s)\partial_t p^{\dagger}(\mathbf{x}, t_1 - t; \mathbf{x}_r)dt. \quad (10)$$

This is produced by the interaction between two wavefields: the wavefield p propagating forward from the emitters $\mathbf{x}_s$, and the adjoint wavefield

$$p^{\dagger}(\mathbf{x}, t) = \frac{1}{N}\int_{t_0}^{t_1} \partial_t p_{\mathrm{obs}}(\mathbf{x}_r, t' + \Delta T)G(\mathbf{x}, t'; \mathbf{x}_r, t)dt' \quad (11)$$

propagating backward in time from the receivers $\mathbf{x}_r$.

Equation (9) establishes the relationship between cross-correlation traveltime shifts and velocity perturbations in terms of the finite-frequency sensitivity kernels $K(\mathbf{x})$ [28], [30], [31]. In principle, the sensitivity kernel in (10) depends on both the observables and model parameters, and it is therefore

a non-linear relationship. However, linearized approaches can be justified for velocity contrasts up to 10% with respect to the background model [37].

A. Linearization

Assume that we represent the velocity distribution of the breast tissue as $c(\mathbf{x}) = c_0 + \delta c(\mathbf{x})$, where c_0 refers to a homogeneous background model (water). If the differences are small such that $|\delta c(\mathbf{x})| \ll c_0$, the observed wavefield $p_{\mathrm{obs}} = p_0 + \delta p$ will be a time shifted version of the background wavefield p_0,

$$p_{\mathrm{obs}}(\mathbf{x}_r, t + \Delta T) \approx p_0(\mathbf{x}_r, t). \qquad (12)$$

For a homogeneous unbounded medium, the 3D Green's function is given by

$$G_0(\mathbf{x}_r, t; \mathbf{x}_s, t') = \frac{1}{4\pi R_{sr}} \delta \left(t - t' - \frac{R_{sr}}{c_0} \right), \qquad (13)$$

where $R_{sr} = \|\mathbf{x}_s - \mathbf{x}_r\|$, and assuming point sources, $f(\mathbf{x}, t) = f(t)\delta(\mathbf{x} - \mathbf{x}_s)$, it follows that

$$p_0(\mathbf{x}_r, t; \mathbf{x}_s) = \frac{1}{4\pi R_{sr}} f \left(t - \frac{R_{sr}}{c_0} \right). \qquad (14)$$

Upon inserting (12) - (14) into (10), we obtain the explicit expression of the linearized traveltime sensitivity kernel K_0,

$$K_0(\mathbf{x}) = \frac{A(\mathbf{x})}{N_L} \int_{t_0}^{t_1} g_1(\mathbf{x}, t) g_2(\mathbf{x}, t) dt, \qquad (15a)$$

$$g_1(\mathbf{x}, t) = \partial_t f \left(t - \frac{R_{xs}}{c_0} \right), \qquad (15b)$$

$$g_2(\mathbf{x}, t) = \partial_t^2 f \left(t_1 - t - \frac{R_{xr} + R_{sr}}{c_0} \right), \qquad (15c)$$

$$A(\mathbf{x}) = \frac{-R_{sr}}{2\pi c_0{}^3 R_{xs} R_{xr}}, \qquad (15d)$$

$$N_L = \int_{t_0}^{t_1} \partial_t f^2 \left(t - \frac{R_{sr}}{c_0} \right) dt, \qquad (15e)$$

where $R_{xs} = \|\mathbf{x} - \mathbf{x}_s\|$ and $R_{xr} = \|\mathbf{x} - \mathbf{x}_r\|$.

Equations (15a) - (15e) define the key ingredient of the forward operator of finite-frequency traveltime tomography, which does neither depend on the unknown model parameters nor on the observed data. Instead, it requires the source-time function $f(t)$, and this can be known, for instance, from the calibration of the scanning device with measurements in water. An example of the finite-frequency sensitivity kernel for a band-limited pulse with frequencies in the range of 1–3 MHz is shown in Fig. 1. Here, for comparison, we also illustrate the equivalent sensitivity predicted from ray theory (dashed line). Unlike the ray-theoretical sensitivities, which are confined to infinitesimally narrow paths, finite-frequency sensitivities extend to finite volumes away from the geometrical ray. They have an ellipsoidal shape defined by the Fresnel zones, with the strongest contribution coming from the first Fresnel zone. Here, the negative sign indicates that a positive velocity perturbation will produce earlier first arrivals. For higher-order Fresnel zones, the sensitivities are oscillatory with alternating signs, and their magnitude decrease

due to destructive interferences between the contribution of individual frequencies. Contrary to ray theory, the sensitivities along the geometrical ray path are zero, which is an effect of the cross-correlation measurements. The entire waveform of the first arrivals contributes to the measured traveltimes, and it is therefore the results of the interference between direct and scattered waves [30]. Higher frequencies produce narrower sensitivity kernels, being consistent with what ray theory predicts. We refer the reader to [45] for a more detailed discussion about the sensitivity kernels.

Our approach uses a homogeneous background model to linearize the parameter-to-observable map. This allows us to obtain analytical expressions for the sensitivity kernels. Finite-frequency tomography, however, can similarly be defined for heterogeneous background media, using (10) and (11) to numerically compute the sensitivities. This can be useful, for instance, to incorporate refraction effects into the method [31].

B. 2D approximation

When the emitters and receivers are located in the same plane, 2D approximations are often applied to accelerate the reconstructions [46]. Assume we discretize the breast tissue using the Cartesian coordinates $\mathbf{x} = [x; y; z]$ with the z-direction orthogonal to the acquisition plane. If the breast tissue shows smooth variations of the velocity in z-direction, at least in the volumes defined by the sensitivity kernels, then $\delta c(\mathbf{x}) \approx \delta c(x, y)$, and the forward problem (9) can be reduced to

$$\delta T \approx \iint_S \left(\int_{z_0}^{z_1} K_0(\mathbf{x}) dz \right) \delta c(x, y) \, dx \, dy, \qquad (16)$$

where S is the ROI located at the acquisition plane, and $[z_0, z_1]$ is the interval in which the main contribution of K_0 occurs. The accuracy of this approximation will depend on both the structure of the breast tissue and the frequencies used. At high frequencies, the sensitivity kernels extend to narrower volumes, and the assumption of smooth variations can be better justified.

C. New parameterization of the forward operator

The combination of (9) and (15), or (16) for 2D approximations, describes the tomographic method presented in this study. Using a compact notation, the linearized forward problem is written as

$$\delta\mathbf{T} = \mathbf{F}\delta\mathbf{c}, \qquad (17)$$

where $\mathbf{F} \in \mathbb{R}^{M \times N}$ is the forward matrix, $\delta\mathbf{T} = [\delta T_1; \ldots; \delta T_M]$, and $\delta\mathbf{c} = [\delta c_1; \ldots; \delta c_N]$. Here, M and N indicate the number of measurements and model parameters, respectively. Each row in $\mathbf{F}$ corresponds to a sensitivity kernel for an emitter-receiver pair. As Fig. 1 suggests, this forward matrix is denser than its equivalent in ray theory. For large-scale problems, the explicit computation of $\mathbf{F}$ may even become prohibitive due to large memory requirements. We circumvent this by encoding the information contained in the sensitivity kernels using a new parameterization. This allows us to solve the inverse problem related to (17) using iterative
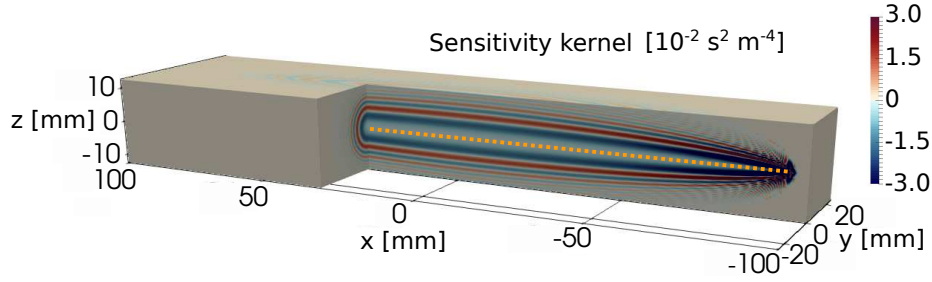
Fig. 1. Sensitivity kernel for a band-limited signal with frequencies in the range of 1–3 MHz. The emitter and the receiver are located at positions (-95,0,0) mm and (95,0,0) mm, respectively. The dashed line indicates the corresponding sensitivity predicted from ray theory.

solvers as, for instance, the LSQR algorithm [47], in which the matrix $\mathbf{F}$ is implicitly given through matrix-vector products.

The pattern shared by the sensitivity kernels can easily be observed in the temporal Fourier domain. We first convert (4) and (5) with the approximation made in (12) [45], [48]:

$$\delta T = -\frac{\mathrm{Re} \int_0^\infty i\omega p(\omega)^* \delta p(\omega) d\omega}{\int_0^\infty \omega^2 p(\omega)^* p(\omega) d\omega}. \tag{18}$$

Here, $p(\omega)$ denotes the Fourier-transformed pressure field, with angular frequency ω, and we omitted the spatial dependency for clarity. The superscript $*$ and Re denote the complex conjugate and the real part of the complex number, respectively.

For a point source $f(\mathbf{x}, \omega) = f(\omega)\delta(\mathbf{x} - \mathbf{x}_s)$, the pressure fields at receiver locations $\mathbf{x}_r$ can be expressed in terms of Green's functions as

$$p(\omega) = f(\omega)G_0(\mathbf{x}_r, \omega; \mathbf{x}_s), \tag{19}$$

$$\delta p(\omega) = -\int_V \frac{2\omega^2 \delta c(\mathbf{x}')}{c_0^3} p(\mathbf{x}', \omega; \mathbf{x}_s)G_0(\mathbf{x}_r, \omega; \mathbf{x}')d\mathbf{x}', \tag{20}$$

where the frequency-domain Green's function is

$$G_0(\mathbf{x}_r, \omega; \mathbf{x}_s) = \frac{1}{4\pi R_{sr}} \exp\left(-i\frac{\omega}{c_0}R_{sr}\right). \tag{21}$$

Upon inserting (19) - (21) into (18), the sensitivity kernel $K_0 = K_0(\mathbf{x})$ takes the form

$$K_0 = A\frac{\int_0^\omega \omega^3 |f(\omega)|^2 \sin\left(\frac{\omega}{c_0}(R_{xs} + R_{xr} - R_{sr})\right) d\omega}{\int_0^\omega \omega^2 |f(\omega)|^2 d\omega}. \tag{22}$$

The term $A = A(\mathbf{x})$ is the same as in (15d), and it mostly accounts for geometrical spreading. Because it does not depend on ω, it can be included in the sensitivity kernels at a later stage. We therefore do not consider it for the new parameterization of the forward operator.

From (22), we see that by defining K_0 in terms of $R = R_{xs} + R_{xr} - R_{sr}$, the sensitivities for any emitter-receiver combination are represented by the same analytical function. We show an example of this in Fig. 2. The function describes the diffraction pattern observed in the sensitivity kernels, that is, the values and locations of the Fresnel zones. Being independent of the emitter-receiver geometry, it essentially encodes the complete forward operator $\mathbf{F}$, without the need of computing it explicitly. Usually, we need very few terms to
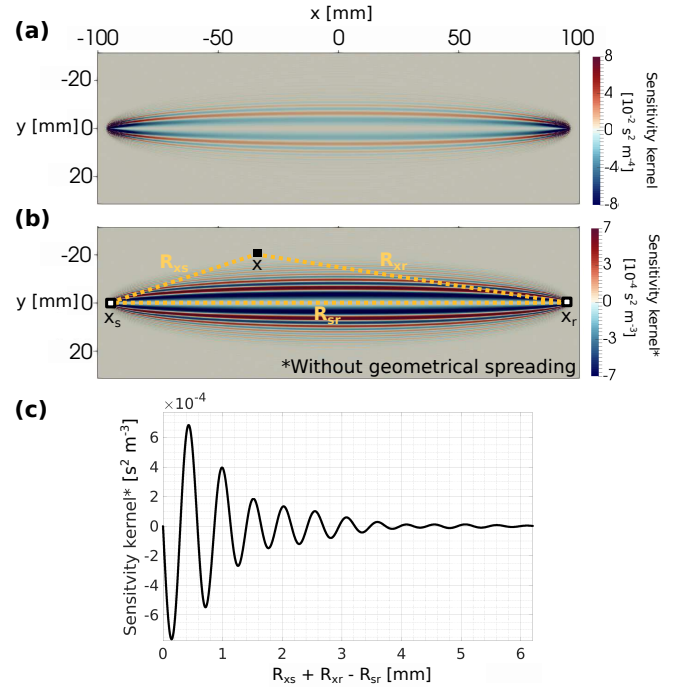

Fig. 2. Cross section in xy-plane of the sensitivity kernel in Fig. 1 (a) with and (b) without the geometrical spreading term $A(\mathbf{x})$. (c) Sensitivity kernel in (b) represented as a function of $R = R_{xs} + R_{xr} - R_{sr}$. These distances are indicated in (b) with dashed lines, together with the positions of the emitter $\mathbf{x}_s$, receiver $\mathbf{x}_r$ and an arbitrary spatial location $\mathbf{x}$.

represent accurately the function in (22), and the sparsity of the forward operator can be controlled by truncating the maximum value of the parameter R. We therefore store the coefficients and arguments of the involved trigonometric functions, and we compute the elements of $\mathbf{F}$ on the fly through the matrix-vector products required during the iterative linear inversion. For each matrix-vector operation, the actual values of the sensitivities are computed by evaluating the analytical function in the discretization grid, and multiplying them by the corresponding geometrical spreading term $A(\mathbf{x})$. These computations can be done very efficiently in GPU architectures, for which trigonometric functions are optimized operations.

D. Inversion and resolution analysis

The inverse problem can be formulated as a least-squares minimization, where we estimate the model parameters that

minimize the objective functional

$$\chi(\delta\mathbf{c}) = \frac{1}{2}\|\mathbf{F}\delta\mathbf{c} - \delta\mathbf{T}_{\text{obs}}\|^2_{\mathbf{\Gamma}^{-1}_{\text{noise}}} + J(\delta\mathbf{c}). \qquad (23)$$

Here, the first term accounts for the discrepancies between the predicted and observed traveltimes, and $J(\delta\mathbf{c})$ is the regularization term. The weighted norm is defined as $\|\mathbf{x}\|^2_{\mathbf{\Gamma}^{-1}} = \mathbf{x}^T\mathbf{\Gamma}^{-1}\mathbf{x}$, and we assume Gaussian noise with zero mean and covariance matrix $\mathbf{\Gamma}_{\text{noise}}$. This may be justified if we minimize large measurement errors by (1) cross-correlating only the time interval of the first arrivals, and (2) avoiding cycle skips by carefully checking for outliers in measurements. We solve the regularized least squares problem (23) iteratively and without explicitly constructing the forward matrix $\mathbf{F}$. Here, we specifically use the implementation provided by [49].

The regularization term incorporates our prior information about the model parameters to mitigate the ill-posed inverse problem, and to ensure meaningful solutions. If the prior is Gaussian with covariance matrix $\mathbf{\Gamma}_{\text{prior}}$, and $J(\delta\mathbf{c}) = \frac{1}{2}\|\delta\mathbf{c}\|^2_{\mathbf{\Gamma}^{-1}_{\text{prior}}}$, the solution can be analytically estimated as

$$\delta\mathbf{c}_{\text{est}} = (\mathbf{H}_{\text{misfit}+\mathbf{\Gamma}^{-1}_{\text{prior}}})^{-1}\mathbf{F}^T\mathbf{\Gamma}^{-1}_{\text{noise}}\delta\mathbf{T}, \qquad (24)$$

where $\mathbf{H}_{\text{misfit}} = \mathbf{F}^T\mathbf{\Gamma}^{-1}_{\text{noise}}\mathbf{F}$ is the Hessian of the data-misfit term. Uncertainties in the solution (24) are described by means of the posterior covariance

$$\mathbf{\Gamma}_{\text{post}} = (\mathbf{H}_{\text{misfit}+\mathbf{\Gamma}^{-1}_{\text{prior}}})^{-1}, \qquad (25)$$

and model resolution matrix

$$\mathbf{R} = (\mathbf{H}_{\text{misfit}+\mathbf{\Gamma}^{-1}_{\text{prior}}})^{-1}\mathbf{H}_{\text{misfit}} \qquad (26)$$

that satisfies $\delta\mathbf{c}_{\text{est}} = \mathbf{R}\delta\mathbf{c}_{\text{true}}$. For a comprehensive analysis and derivations of these equations the reader is referred to [50].

For large-scale problems, even when $\mathbf{F}$ is explicitly available, computing $\mathbf{\Gamma}_{\text{post}}$ and $\mathbf{R}$ may be challenging. However, we can benefit from the rapidly decaying eigenvalues of $\mathbf{\Gamma}^{1/2}_{\text{prior}}\mathbf{H}_{\text{misfit}}\mathbf{\Gamma}^{1/2}_{\text{prior}}$ to compute their low-rank approximations [51]. We do this by retaining the $k < N$ largest eigenvalues and the corresponding eigenvectors. That is, we approximate

$$\mathbf{\Gamma}^{1/2}_{\text{prior}}\mathbf{H}_{\text{misfit}}\mathbf{\Gamma}^{1/2}_{\text{prior}} = \mathbf{V}\mathbf{\Lambda}\mathbf{V}^T \approx \mathbf{V}_k\mathbf{\Lambda}_k\mathbf{V}_k^T, \qquad (27)$$

where $\mathbf{\Lambda} = \text{diag}(\lambda_i) \in \mathbb{R}^{N \times N}$ and $\mathbf{V} \in \mathbb{R}^{N \times N}$ are the eigenvalue and eigenvector matrix, respectively. Here, $\mathbf{\Lambda}_k \in \mathbb{R}^{k \times k}$ and $\mathbf{V}_k \in \mathbb{R}^{N \times k}$ represent the truncated eigenvalue and eigenvector matrices. Then, the low-rank approximations of $\mathbf{\Gamma}_{\text{post}}$ and $\mathbf{R}$ are given by

$$\mathbf{\Gamma}_{\text{post}} \approx \mathbf{\Gamma}^{1/2}_{\text{prior}}\left(\mathbf{I} - \mathbf{V}_k\mathbf{D}_k\mathbf{V}_k^T\right)\mathbf{\Gamma}^{1/2}_{\text{prior}}, \qquad (28)$$

$$\mathbf{R} \approx \mathbf{\Gamma}^{1/2}_{\text{prior}}\mathbf{V}_k\mathbf{D}_k\mathbf{V}_k^T\mathbf{\Gamma}^{-1/2}_{\text{prior}}. \qquad (29)$$

with $\mathbf{D}_k = \text{diag}\left(\frac{\lambda_i}{\lambda_i+1}\right) \in \mathbb{R}^{k \times k}$. For a more detailed derivation of (28) and (29), the reader is referred to [51]. Whereas the derivations above assume Gaussian priors, they may still provide useful information about resolution and uncertainties when non-Gaussian priors are used for reconstructions. The regularization term mostly acts in the effective nullspace of the data-misfit Hessian, and this is removed by applying low-rank approximations.

The posterior covariance $\mathbf{\Gamma}_{\text{post}}$ is useful to interpret the reliability of our velocity estimations. The diagonal entries indicate the variances of the individual parameters, and the off-diagonal entries show the correlations between the errors in different model parameters. As observed in (28), $\mathbf{\Gamma}_{\text{post}}$ is the result of extracting from our prior uncertainties the information we gain from the data.

The resolution matrix $\mathbf{R}$ indicates how well the model parameters are resolved in the inversion. It assumes that the observed data fully satisfy the forward problem, and when the model parameters are perfectly resolved, $\mathbf{R}$ equals the identity matrix. In general, however, $\mathbf{R} \neq \mathbf{I}$, and the estimated parameters are weighted averages of the true parameters. Each column of $\mathbf{R}$ is interpreted as a point-spread function (PSF), which illustrates the blurring of one parameter into others. PSFs are therefore useful to describe how independently an individual parameter can be resolved by the data.

For high-dimensional problems, the low-rank approximation of $\mathbf{R}$ may still be prohibitively expensive to compute. Alternatively, we can estimate PSFs from the data-misfit Hessian $\mathbf{H}_{\text{misfit}}$ [52]. From the definition of $\mathbf{R}$, we observe that

$$\delta\mathbf{c}_{\text{est}} = \mathbf{R}\delta\mathbf{c}_{\text{true}} = (\mathbf{H}_{\text{misfit}} + \mathbf{\Gamma}^{-1}_{\text{prior}})^{-1}\mathbf{H}_{\text{misfit}}\delta\mathbf{c}_{\text{true}}. \qquad (30)$$

Here, the term $\mathbf{H}_{\text{misfit}}\delta\mathbf{c}_{\text{true}}$ indicates the direction of the model updates. When this is multiplied by $(\mathbf{H}_{\text{misfit}} + \alpha\mathbf{\Gamma}^{-1}_{\text{prior}})^{-1}$, we converge to the solution in a single iteration. If we apply $\mathbf{H}_{\text{misfit}}$ to a point-localized model perturbation $\delta\mathbf{c}$, it will therefore provide a conservative estimation of the PSFs. In our study, we use this approach for the resolution analysis of the finite-frequency traveltime tomography, and in particular, to understand how the vertical resolution is related to the acquisition design.

III. 2D LAB DATA APPLICATION

We consider the dataset provided by the Spanish National Research Council (CSIC) and the Complutense University of Madrid (UCM) as part of the *SPIE USCT Data Challenge 2017* [53], [54]. The experimental setup used for the measurements is shown in Fig. 3. The acquisition system consists of two 16-element linear transducer arrays. The elements in one array act as emitters with a central frequency of 3.2 MHz and bandwidth of 50%, while the others are receiving. To acquire transmission data, the receiving array is placed in 11 different positions per position of the emitting array. The whole system is rotated 23 times with respect to the vertical axis describing a circle of 95 mm radius and providing a total of 64768 A-scans. In this way, the emitting array covers 360° without any gap. The last rotation, however, produces a partial overlap between the first and last positions of the emitting array. The maximum data coverage is obtained in a circular ROI of 70 mm radius, indicated in gray in Fig. 3. The same figure also illustrates the cylindrical phantom used for the measurements. It is based on water, gelatine, alcohol and graphite powder, and it includes an homogeneous background of 94 mm diameter,
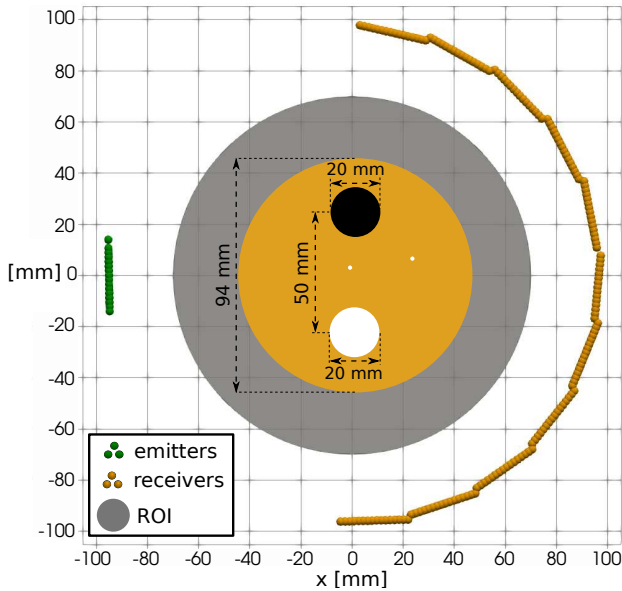
Fig. 3. Acquisition system and an illustration of the tissue mimicking phantom used for the lab measurements. The phantom contains two inclusions of low (black circle) and high (white circle) velocity, and two steel needles (white dots). Here the colors do not have a quantitative meaning.

Fig. 4. (a) 2D velocity reconstruction and (b) normalized sensitivity coverage. Both images only show the ROI indicated in gray in Fig. 3.

two inclusions of 20 mm diameter, and two steel needles of 0.25 mm diameter. The phantom is submerged in water with a calibrated velocity of 1479.7 m/s.

Although the experiment is inherently 3D, the lack of vertical variation in acoustic properties of the phantom makes 2D approximations reasonable. Fig. 4(a) shows the velocity reconstruction obtained using the 2D forward problem in (16). Here, and hereafter, we apply total variation regularization [49], and we test different values of the regularization parameter to select the most suitable one. We discretize the model parameters using a rectilinear grid with 1 mm mesh size. This gives a total of 15373 unknowns in the ROI, and thus, a forward operator with dimensions 64768×15373. Despite the over-determined nature of the problem, redundancies exist due to imperfect data coverage, and the inverse problem is ill-posed (see Fig. 5(a)). By summing the absolute values of the rows in the forward operator, we also compute the sensitivity coverage of the experiment, shown in Fig. 4(b). We observe that the coverage decreases towards the center of the ROI, which is a consequence of the approximately regular distribution of the transducers [55], [56]. The region with highest coverage in the left side is caused by the overlapped positions of transducers in the last rotation of the acquisition system.

Our reconstruction recovers accurately both velocity heterogeneities and the homogeneous background of the phantom. First-arrival traveltimes do not contain information about the needles, which act as scatterers, and they are therefore invisible for transmission tomography. Empirical velocity measurements of the true phantom are not available, and this excludes a quantitative assessment of our velocity estimations. Yet, our results are in agreement with the reconstructions obtained by other groups [53], which certainly shows the efficiency of our imaging method. Whereas both inclusions have the same
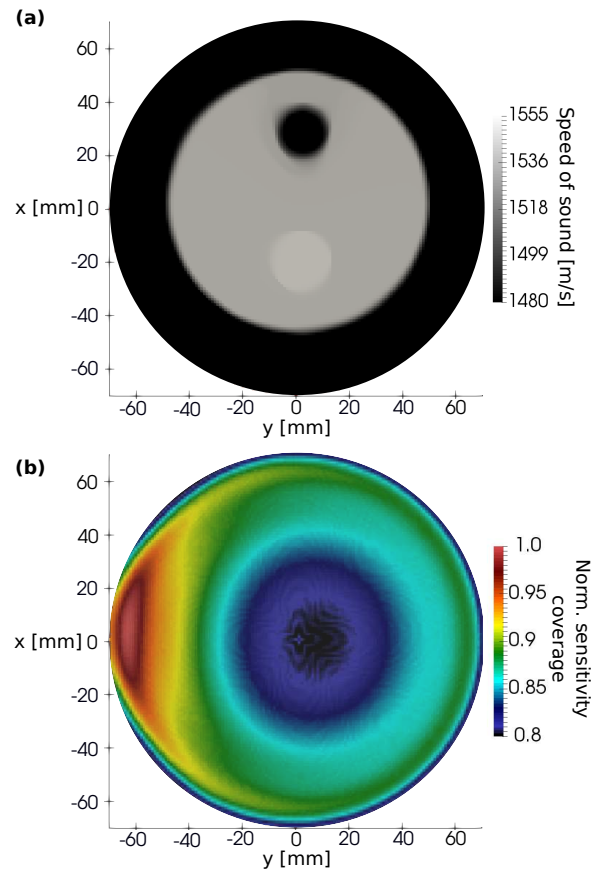
size, a closer look to our reconstruction reveals that the high velocity inclusion is slightly bigger than the low velocity one. This may be an effect of our linearization approximation, in which the sensitivity kernels are computed in an homogeneous model, and therefore, they neglect the bending that occurs in heterogeneous media. Compared to straight-ray tomography, however, the size of the low velocity inclusion is more accurately recovered by our method. A comparison of results obtained by both methods is shown in [57].

To assess the quality of our solution, a comparison between the true model and the solution might be insufficient. Although this suggests that the main features of the true phantom are well resolved, it obscures the actual contribution of our prior knowledge introduced by the choice of the regularization. For this example a comprehensive analysis of the resolution is available. We compute the singular value spectrum of the forward operator, shown in Fig. 5(a). As we observe, the singular values decay rapidly in magnitude, suggesting that the data only contain information about few effective model parameters. We truncate the singular value spectrum after a decrease of three orders of magnitude and consider values below as the effective nullspace. We therefore retain 3000 singular values, and we compute low-rank approximations of the posterior covariance and resolution matrices, see (28) and (29), respectively. Here, we assume equally reliable observations, i.e., $\mathbf{\Gamma}_{\text{noise}} = \sigma_p^{-2}\mathbf{I}$ with $\sigma_p = 2.5 \cdot 10^{-8}$ s being the
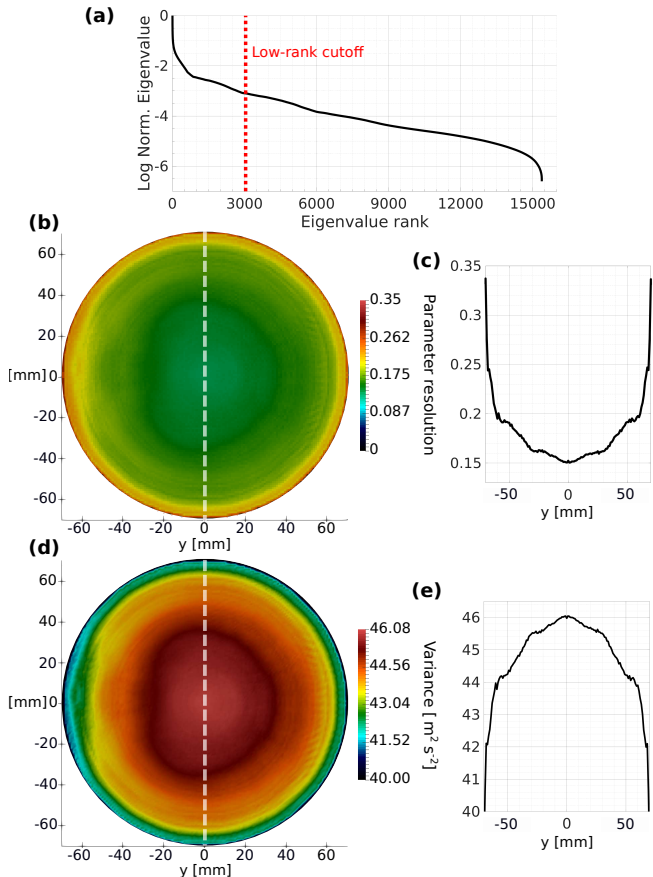
Fig. 5. (a) Singular value spectrum of the 2D forward operator. The red line indicates the low-rank cutoff used to approximate the resolution and posterior covariance matrices. (b), (c) Diagonal elements of the resolution matrix and a cross section at the position indicated by the dashed white line, respectively. (d), (e) Diagonal elements of the posterior covariance matrix and a cross section at $y = 0$ mm, respectively.

minimum cross-correlation time shift that can be measured. The diagonal elements of these matrices are shown in Figs. 5(b) and 5(d), respectively. To better understand the images, we moreover show their cross sections at $y = 0$ mm in Figs. 5(c) and 5(e). For both quantities we observe similar features: the parameter resolution decreases gradually, and the variances increase towards the center of the ROI. This means that we are more uncertain about the parameters resolved at the center of the ROI, which corresponds to the observations made in the sensitivity coverage.

The diagonal elements of the resolution matrix are useful to understand where we may expect better resolved parameters. However, it misses useful information encoded in the off-diagonal elements about trade-offs and spatial correlations between parameters that occur due to imperfect data coverage. In Fig. 6(a), we represent few columns of the resolution matrix, which describe the blurring effect introduced by the inverse operator. These are the PSFs associated to point-localized unit perturbations at positions $(x, y) = (0, 0), (0, 20), (0, 40), (0, 60)$ mm and $(-60, 0)$, $(-40, 0), (-20, 0)$ mm. Our resolution analysis reveals that the smearing mainly extends to circular areas of 1 mm radius. The worst resolution is obtained at the center of ROI, and the

trade-offs decrease in spatial extension towards its boundary. Similar behaviour is observed in the amplitude of the PSFs.

The information extracted from the resolution matrix corresponds to an idealized situation, and it may lead us to rather optimistic conclusions. It assumes that (1) the observed data satisfy exactly the forward problem in (17), and (2) our model estimation fully converges to the solution. For 3D problems the computation of the resolution matrix becomes prohibitive, and therefore, PSFs can only be estimated through Hessian-vector products (see (30)). These quantities, which indicate the direction of the single-iteration model update, are considered as conservative estimations of PSFs [52], [58]. Here we compare both results in order to gain deeper understanding for the following sections.

The estimations of the PSFs using Hessian-vector products are shown in Fig. 6(b) for the same locations as before. As expected, the parameter trade-offs extend to wider areas than the ones estimated using the resolution matrix. This may be a consequence of the projection of the 3D sensitivities to the x-y plane, which is intrinsic to our definition of the 2D forward problem (see (16)). Although the trade-offs are mainly localized in a circle of 5 mm radius around the positions of the perturbations, the locations of the most significant values agree with our observations in Fig. 6(a). In fact, the principal difference between Figs. 6(a) and 6(b) is due to the normalization factor in (30). PSFs estimated by Hessian-vector products are dominated by smoother eigenvectors associated to largest eigenvalues. Consequently, they obscure the small-scale features provided by other eigenvectors that the inverse operator resolves.

IV. 3D RECONSTRUCTION WITH 2D LAB DATASET

Lab experiments are 3D in nature, and volumetric reconstructions may be preferable, especially when the observations are sensitive to regions with vertically varying structure. In this section, we use the same dataset as in the example before to illustrate the potential of our method to image out of plane.

We apply the forward problem in (9) to reconstruct the 3D velocity distribution. The result is shown in Fig. 7(a), and it proves that indeed finite-frequency tomography is capable of providing volumetric images from 2D acquisition systems. In general, our estimated velocity model recovers the main features of the true phantom, with similar accuracy as in the 2D example. The vertical width of the reconstruction corresponds to the region with the highest sensitivity coverage. This is controlled by the interaction of the first Fresnel zone of the sensitivities corresponding to each emitter-receiver combination. In this application, the maximum Fresnel width is $\sqrt{\frac{c_0 L_{\max}}{f_c}} = 9.4$ mm, where $c_0 = 1479.7$ m/s is the background water velocity, $L_{\max} = 190$ mm is the maximum emitter-receiver distance, and $f_c = 3.2$ MHz is the dominant frequency of the emitting signal. The vertical thickness of our reconstruction will therefore be constrained by this value.

To better understand the quality of our reconstruction, we compute a collection of PSFs estimated by Hessian-vector products. These are visualized in Fig. 7(b) as vertical and horizontal cross sections. The results reveal a similar horizontal
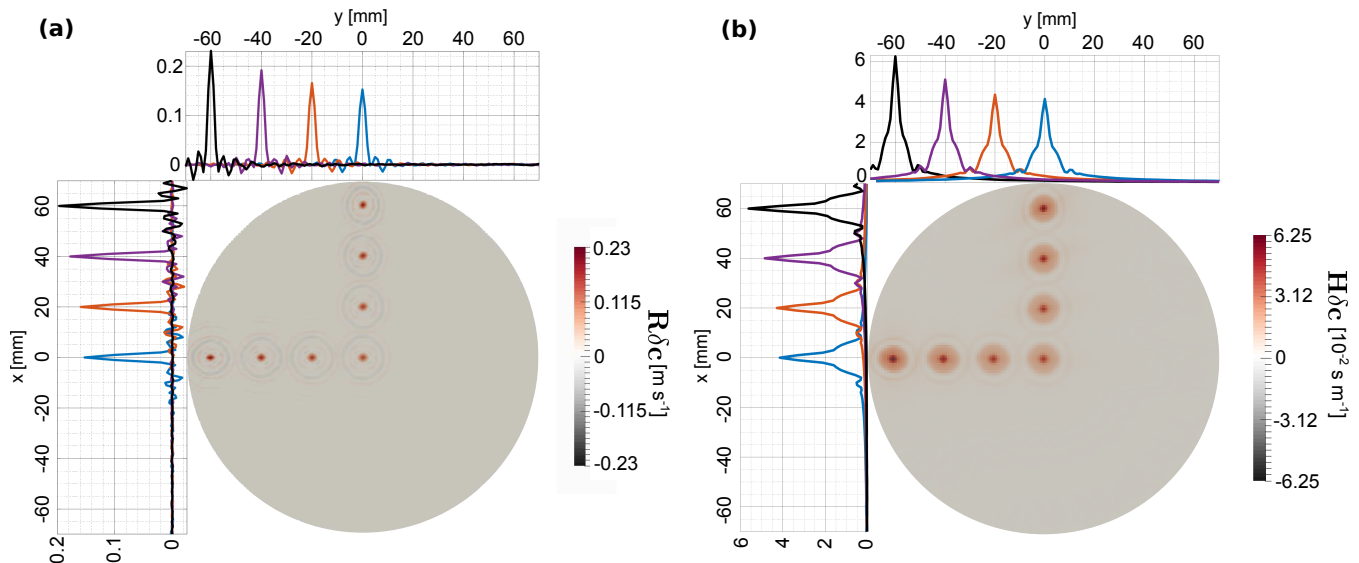
Fig. 6. PSFs corresponding to point-localized unit perturbations at positions $(x, y) = (0, 0)$, $(0, 20)$, $(0, 40)$, $(0, 60)$, $(-60, 0)$, $(-40, 0)$, $(-20, 0)$ mm. These are estimated using (a) the resolution matrix, and (b) Hessian-vector products. In both figures we show the horizontal and vertical cross sections at $y = 0$ mm and $x = 0$ mm, respectively.

resolution as in the 2D example, but a poor vertical resolution that essentially makes velocity parameters indistinguishable in z-direction. As mentioned before, its extent comprises the most covered region of approximately 8 mm width, and it remains constant along the horizontal direction. In this example, the lack of crossing sensitivity kernels in z-direction decreases our ability to constrain independently the parameters.

V. SIMULATED FULL 3D EXPERIMENT: SLICE-BY-SLICE ACQUISITION

To improve the vertical resolution of an experiment, it is essential to provide measurements with crossing or overlapping sensitivities. For the previous experiment, this can be done, for instance, by collecting additional measurements at different elevations. Because the phantom has cylindrical symmetry, we simulate a slice-by-slice acquisition, and we assume that the same data have been recorded at different elevations. The aim of this example is twofold: on one hand, we want to show that finite-frequency tomography is a powerful tool to provide consistent full 3D images from slice-by-slice acquisition systems; and on the other hand, we want to investigate the conditions for a meaningful vertical resolution. We relate the latter to the vertical spacing between different elevations.

In our previous result, we observed a vertical resolution of approximately 8 mm. Following this, we compare experiments using a vertical spacing of 3 mm and 8 mm. The first spacing ensures the overlapping of the sensitivities at different elevations, and the second one only avoids gaps between them. Fig. 8 shows the reconstructions for both cases, in which the ROI is a cylinder with radius 70 mm and height 32 mm. For Fig. 8(a) we translate the scanning system to 11 positions in $z \in [-23, 23]$ mm, and Fig. 8(b) has 7 positions in $z \in [-24, 24]$ mm. In both cases, our method successfully recovers the cylindrical 3D phantom, including both heterogeneities. Because current methods using these

acquisition systems obtain 3D breast images by stacking 2D reconstructed slices [59], our results constitute a fundamental advance in this context.

The experiment with the largest spacing introduces oscillations in the shapes of the recovered heterogeneities. To understand this better, we compute PSFs and analyze differences in local resolution for both experiments, shown in Fig. 9. As expected, the PSFs computed for 8 mm spacing are equivalent to those already observed in Fig. 7. However, the vertical cross sections demonstrate that the resolution length can significantly be reduced when the sensitivities overlap. We illustrate this in Fig. 9(c), where we plot 1D cross sections of PSFs due to a perturbation at $x = 0$ mm. The response is remarkably sharper for 3 mm spacing meaning that the parameters in vertical direction are better constraint. Although we also observe relatively strong side lobes in the responses, these become weaker towards the center of the ROI, where the sensitivities from different elevations overlap most. Horizontal cross-sections also show an interesting effect, see Fig. 9(d). PSFs for 3 mm have an increased contrast and trade-offs that decrease in spatial extent.

VI. DISCUSSION AND CONCLUSIONS

This work presents a new transmission tomography method to estimate velocity variations in breast tissue using ultrasound data. It minimizes cross-correlation traveltime shifts between the observations and calibration data in water, being internally consistent with the standard procedure of traveltime estimations. The actual measurements are band-limited and include finite-frequency effects of the cross-correlated pulses. Contrary to what ray theory predicts, finite-frequency traveltimes are affected by scattering and diffraction effects off the ray path, and their sensitivity to velocity variations therefore extends to ellipsoidal volumes. In the context of transmission tomogra-
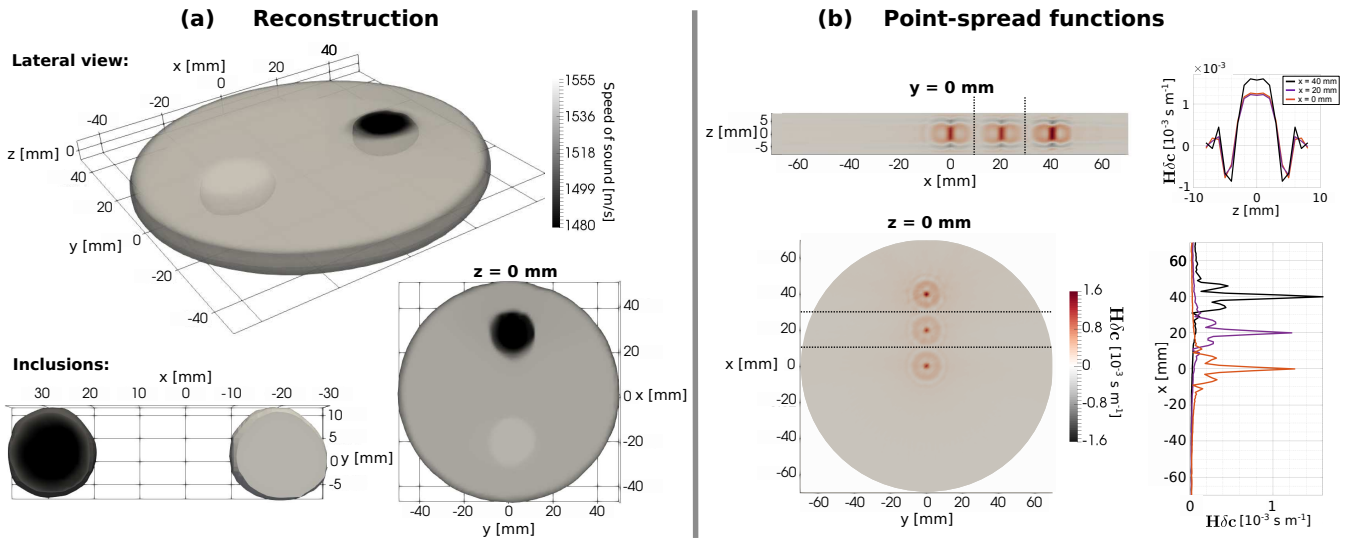
Fig. 7. (a) 3D velocity reconstruction using the same dataset as in the 2D example. We show the lateral view of the volumetric reconstruction, the top view of the isolated inclusions, and a cross section at $z = 0$ mm. We reduce the opacity of the first image to visualize the inclusions. (b) Estimations of PSFs due to unit perturbations at locations $(x, y, z) = (0, 0, 0), (20, 0, 0), (40, 0, 0)$ mm. We show the 2D and 1D cross sections in vertical and horizontal directions. Dashed lines indicate that PSFs are computed individually, although we visualize all in the same image.
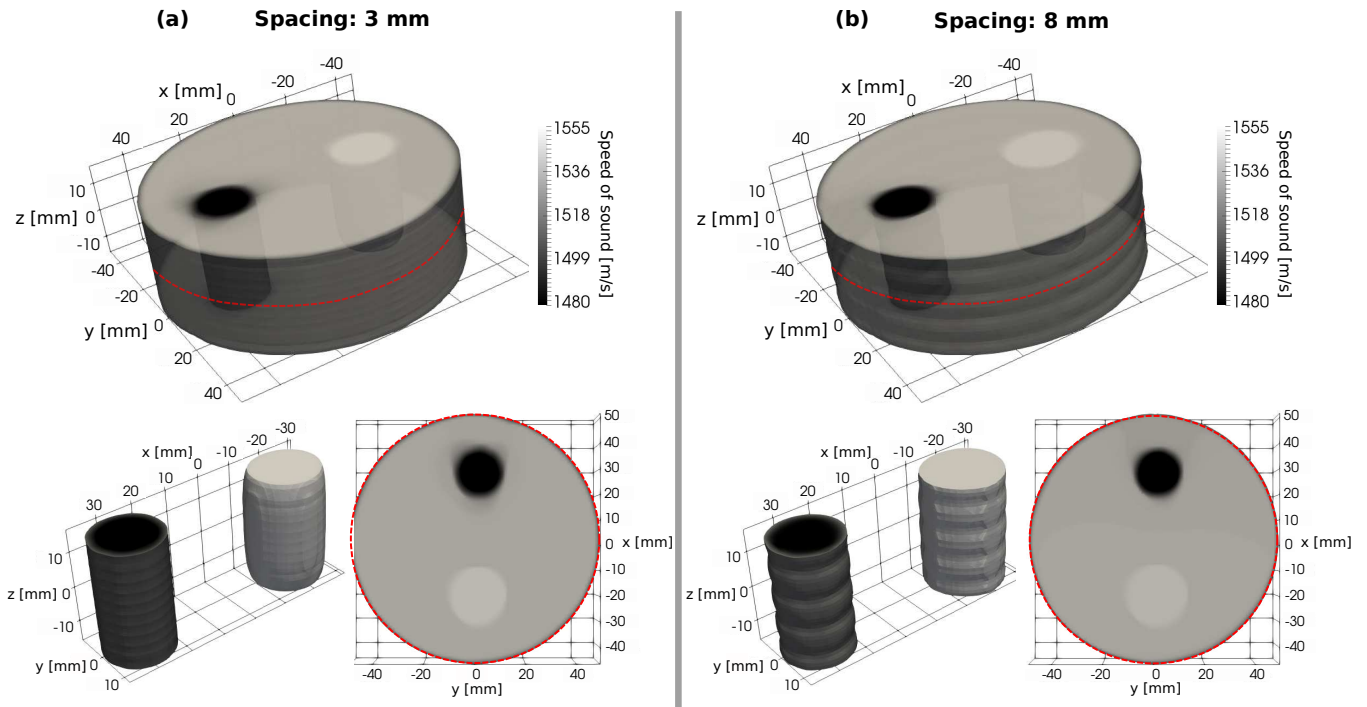

Fig. 8. 3D velocity reconstruction for (a) 3 mm and (b) 8 mm spacing between measurements at different elevations. We show in each case the lateral view, the isolated view of the inclusions and the cross section at $z = 0$ mm. The red lines indicate the positions of the cross sections.

phy, this work represents a natural extension of ray theory to finite-frequency waves.

Finite-frequency tomography has been extensively studied in seismology. It is best suited for experiments with (1) velocity variations that are under 10% [37] and therefore quasi-linearly related to traveltime differences, (2) sufficient waveform similarity between cross-correlated waves, and (3) dense data coverage. In breast imaging with USCT, all these conditions are satisfied, therefore suggesting an ideal field of application for this method.

Though being methodologically more involved than ray-based tomography, finite-frequency tomography has two major advantages. First and foremost, it correctly accounts for the frequency dependence of traveltime measurements. From a data perspective, this means that traveltime measurements may in fact be made in multiple frequency bands in order to capture the dispersive nature of waves travelling through heterogeneous and dissipative media. While being beyond the scope of this study, such multiple-frequency measurements may greatly enlarge the dataset, thereby improving tomographic resolution
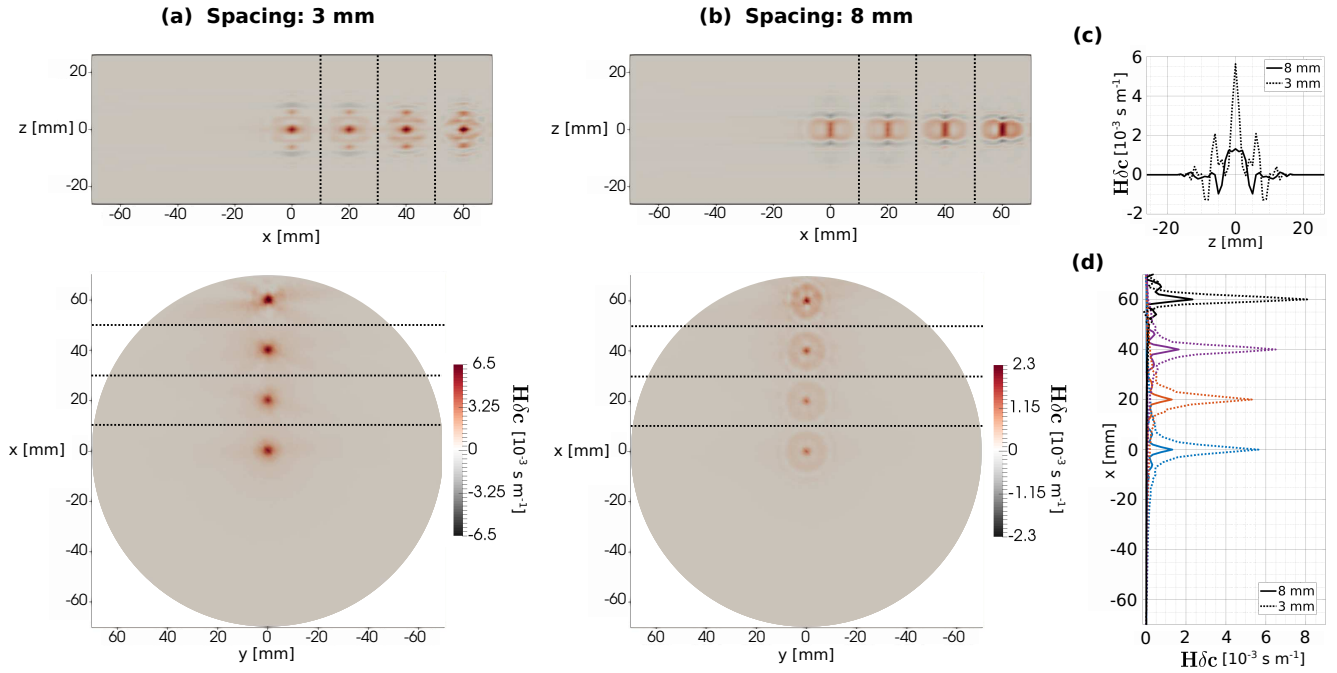
(a) Spacing: 3 mm　　　　**(b) Spacing: 8 mm**

Fig. 9. (a), (b) Vertical and horizontal cross sections of PSFs due to perturbations at $(x, y, z) = (0, 0, 0)$, $(20, 0, 0)$, $(40, 0, 0)$, $(60, 0, 0)$ mm for 3 mm and 8 mm spacing, respectively. (c) Vertical 1D cross section of PSFs due to a perturbation at $x = 0$ mm. (d) Horizontal 1D cross sections of PSFs at $y = 0$ mm.

[34]. From an inversion perspective, the computation of correct finite-frequency sensitivities helps to avoid inversion artifacts related to the approximation of sensitivities. For instance, the approximation by infinitely thin rays may in fact lead to unrealistically good resolution by virtue of the central slice theorem [60]. In this context, the non-zero width of finite-frequency kernels naturally limits resolution to what is physically possible by using waves with a certain frequency content.

The second main advantage, specifically in medical ultrasound, is the ability to produce 3D images based on 2D acquisition systems. Slice-by-slice acquisition devices have gained popularity due to their fast reconstructions. However, they often suffer from artifacts caused by the 2D approximations of inherently 3D wave phenomena [21]–[24]. Our work demonstrates that finite-frequency tomography does not only offer the possibility to image out of plane, but also to better constrain acoustic parameters by coupling data from different slices. This is a fundamental improvement compared to the current approaches, in which pseudo-volumetric images are built by stacking 2D coronal slices [59]. By using more accurate physical modelling, our approach respects the finite-frequency nature of the data, thereby reducing artifacts caused by 2D projections. Furthermore, it avoids subjective choices related to the post-processing of reconstructed images. In this sense, this work makes the critical contribution of providing truly 3D reconstructions using slice-by-slice devices, which may be important to accurately locate tissue anomalies inside the breast volume.

A prerequisite of our method is access to calibration data that ensure sufficient waveform similarity between cross-correlated waves. A direct consequence of waveform similarity

is the possibility to compute the Jacobian operator at any frequency analytically, without suffering from time consuming numerical wave propagation simulations. The resulting linear inverse problem is very attractive for clinical practice, where fast and accurate solutions are indispensable for the recurring experiments. The possibility to compute properties of the forward operator prior to any experiment reduces the time to solution significantly.

To further reduce computational cost, we develop a 1D parameterization that allows us to represent any finite-frequency sensitivity kernel, independent of the emitter-receiver configuration, with the same analytic function. It encodes the full Jacobian operator, and we compute its elements on the fly for the matrix-vector operations required in each iteration of the least-squares solver. Our approach is ideal for GPU implementation, and, being matrix-free, it extends very efficiently to large-scale 3D problems. The latter is probably the most interesting application for USCT.

In addition to the tomographic method, we apply a resolution analysis based on PSFs estimations. This is useful for a comparative assessment of the spatial resolution and inter-parameter trade-offs that arise from different experimental setups. For a quantitative interpretation of our results, we require better descriptions of the observational and forward modelling uncertainties, which can only be obtained with further experimental studies.

discussions. The data used in this work are freely available in the *USCT Data Challenge 2017* online platform http://ipeusctdb1.ipe.kit.edu/~usct/challenge/.

REFERENCES

[1] A. T. Stavros, D. Thickman, C. L. Rapp, M. A. Dennis, S. H. Parker, and G. A. Sisney, "Solid breast nodules: use of sonography to distinguish between benign and malignant lesions." *Radiology*, vol. 196, no. 1, pp. 123–134, 1995, pMID: 7784555. [Online]. Available: https://doi.org/10.1148/radiology.196.1.7784555

[2] J. F. Greenleaf, S. A. Johnson, and R. C. Bahn, "Quantitative cross-sectional imaging of ultrasound parameters," in *1977 Ultrasonics Symposium*, Oct 1977, pp. 989–995.

[3] P. Carson, C. Meyer, A. Scherzinger, and T. Oughton, "Breast imaging in coronal planes with simultaneous pulse echo and transmission ultrasound," *Science*, vol. 214, no. 4525, pp. 1141–1143, 1981. [Online]. Available: https://science.sciencemag.org/content/214/4525/1141

[4] T. D. Mast, "Empirical relationships between acoustic parameters in human soft tissues," *Acoustics Research Letters Online*, vol. 1, no. 2, pp. 37–42, 2000. [Online]. Available: https://doi.org/10.1121/1.1336896

[5] M. Sak, N. Duric, P. Littrup, L. Bey-Knight, H. Ali, P. Vallieres, M. E. Sherman, and G. L. Gierach, "Using speed of sound imaging to characterize breast density," *Ultrasound in Medicine and Biology*, vol. 43, no. 1, pp. 91 – 103, 2017. [Online]. Available: http://www.sciencedirect.com/science/article/pii/S0301562916302575

[6] J. A. Harvey and V. E. Bovbjerg, "Quantitative assessment of mammographic breast density: Relationship with breast cancer risk," *Radiology*, vol. 230, no. 1, pp. 29–41, 2004, pMID: 14617762. [Online]. Available: https://doi.org/10.1148/radiol.2301020870

[7] S. Li, M. Jackowski, D. P. Dione, T. Varslot, L. H. Staib, and K. Mueller, "Refraction corrected transmission ultrasound computed tomography for application in breast imaging," *Medical Physics*, vol. 37, no. 5, pp. 2233–2246, 2010. [Online]. Available: https://aapm.onlinelibrary.wiley.com/doi/abs/10.1118/1.3360180

[8] M. Pérez-Liva, J. L. Herraiz, L. Medina-Valdés, J. Camacho, C. Fritsch, B. E. Treeby, and J. M. Udías, "Regularization of image reconstruction in ultrasound computed tomography," in *2015 IEEE Nuclear Science Symposium and Medical Imaging Conference (NSS/MIC)*, Oct 2015, pp. 1–3.

[9] H. Gemmeke, T. Hopp, M. Zapf, C. Kaiser, and N. V. Ruiter, "3D ultrasound computer tomography: Hardware setup, reconstruction methods and first clinical results," *Nuclear Instruments and Methods in Physics Research Section A: Accelerators, Spectrometers, Detectors and Associated Equipment*, vol. 873, pp. 59 – 65, 2017, imaging 2016. [Online]. Available: http://www.sciencedirect.com/science/article/pii/S0168900217307593

[10] J. Tong, F. A. Dahlen, G. Nolet, and H. Marquering, "Diffraction effects upon finite-frequency travel times: A simple 2-D example," *Geophysical Research Letters*, vol. 25, pp. 1983–1986, 1998.

[11] P. R. Williamson, "A guide to the limits of resolution imposed by scattering in ray tomography," *Geophysics*, vol. 56, no. 2, pp. 202–207, 1991. [Online]. Available: https://doi.org/10.1190/1.1443032

[12] J. Wiskin, D. T. Borup, S. A. Johnson, and M. Berggren, "Non-linear inverse scattering: High resolution quantitative breast tissue tomography," *The Journal of the Acoustical Society of America*, vol. 131, no. 5, pp. 3802–3813, 2012. [Online]. Available: https://doi.org/10.1121/1.3699240

[13] R. J. Lavarello and A. J. Hesford, "Methods for forward and inverse scattering in ultrasound tomography," in *Quantitative Ultrasound in Soft Tissues*, J. Mamou and M. L. Oelze, Eds. Dordrecht: Springer Netherlands, 2013, pp. 345–394.

[14] M. André, J. Wiskin, and D. Borup, "Clinical results with ultrasound computed tomography of the breast," in *Quantitative Ultrasound in Soft Tissues*, J. Mamou and M. L. Oelze, Eds. Dordrecht: Springer Netherlands, 2013, pp. 395–432.

[15] N. Ozmen, R. Dapp, M. Zapf, H. Gemmeke, N. V. Ruiter, and K. W. A. van Dongen, "Comparing different ultrasound imaging methods for breast cancer detection," *IEEE Transactions on Ultrasonics, Ferroelectrics, and Frequency Control*, vol. 62, no. 4, pp. 637–646, April 2015.

[16] R. G. Pratt, L. Huang, N. Duric, and P. Littrup, "Sound-speed and attenuation imaging of breast tissue using waveform tomography of transmission ultrasound data," *Proc. SPIE*, vol. 6510, p. 65104S, 2007.

[17] M. Pérez-Liva, J. L. Herraiz, J. M. Udías, E. Miller, B. T. Cox, and B. E. Treeby, "Time domain reconstruction of sound speed and attenuation in ultrasound computed tomography using full wave inversion," *The Journal of the Acoustical Society of America*, vol. 141, no. 3, pp. 1595–1604, 2017. [Online]. Available: https://doi.org/10.1121/1.4976688

[18] C. Boehm, N. Korta Martiartu, N. Vinard, I. J. Balic, and A. Fichtner, "Time-domain spectral-element ultrasound waveform tomography using a stochastic quasi-Newton method," *Proc. SPIE*, vol. 10580, pp. 10 580 – 10 580 – 9, 2018. [Online]. Available: https://doi.org/10.1117/12.2293299

[19] O. C. Agudo, L. Guasch, P. Huthwaite, and M. Warner, "3D imaging of the breast using full-waveform inversion," in *Proceedings of the International Workshop on Medical Ultrasound Tomography: 1.-3. Nov. 2017, Speyer, Germany*. KIT Scientific Publishing, 2018, p. 99.

[20] G. Y. Sandhu, C. Li, O. Roy, S. Schmidt, and N. Duric, "Frequency domain ultrasound waveform tomography: breast imaging using a ring transducer," *Physics in Medicine & Biology*, vol. 60, no. 14, p. 5381, 2015. [Online]. Available: http://stacks.iop.org/0031-9155/60/i=14/a=5381

[21] R. J. Lavarello and M. L. Oelze, "Tomographic reconstruction of three-dimensional volumes using the distorted born iterative method," *IEEE Transactions on Medical Imaging*, vol. 28, no. 10, pp. 1643–1653, Oct 2009.

[22] A. Goncharsky, S. Y. Romanov, and S. Y. Seryozhnikov, "A computer simulation study of soft tissue characterization using low-frequancy ultrasonic tomography," *Ultrasonics*, vol. 67, pp. 136–150, 2016.

[23] J. W. Wiskin, D. T. Borup, E. Iuanow, J. Klock, and M. W. Lenox, "3-D Nonlinear Acoustic Inverse Scattering: Algorithm and Quantitative Results," *IEEE Transactions on Ultrasonics, Ferroelectrics, and Frequency Control*, vol. 64, no. 8, pp. 1161–1174, Aug 2017.

[24] G. Y. Sandhu, E. West, C. Li, O. Roy, and N. Duric, "3D frequency-domain ultrasound waveform tomography breast imaging," *Proc. SPIE*, vol. 10139, pp. 10 139 – 10 139 – 14, 2017. [Online]. Available: https://doi.org/10.1117/12.2254399

[25] R. G. Pratt, "Medical ultrasound tomography: lessons from exploration geophysics," in *Proceedings of the International Workshop on Medical Ultrasound Tomography: 1.-3. Nov. 2017, Speyer, Germany*. KIT Scientific Publishing, 2018, p. 65.

[26] O. Gauthier, J. Virieux, and A. Tarantola, "Two-dimensional nonlinear inversion of seismic waveforms: Numerical results," *Geophysics*, vol. 51, no. 7, pp. 1387–1403, 1986.

[27] C. Bunks, F. M. Saleck, S. Zaleski, and G. Chavent, "Multiscale seismic waveform inversion," *Geophysics*, vol. 60, no. 5, pp. 1457–1473, 1995.

[28] Y. Luo and G. T. Schuster, "Wave-equation traveltime inversion," *Geophysics*, vol. 56, no. 5, pp. 645–653, 1991. [Online]. Available: https://doi.org/10.1190/1.1443081

[29] K. Yomogida, "Fresnel zone inversion for lateral heterogeneities in the Earth," *Pure and Applied Geophysics*, vol. 138, pp. 391–406, 1992.

[30] H. Marquering, F. Dahlen, and G. Nolet, "Three-dimensional sensitivity kernels for finite-frequency traveltimes: the banana-doughnut paradox," *Geophysical Journal International*, vol. 137, no. 3, pp. 805–815, 1999. [Online]. Available: https://onlinelibrary.wiley.com/doi/abs/10.1046/j.1365-246x.1999.00837.x

[31] F. A. Dahlen, G. Nolet, and S.-H. Hung, "Fréchet kernels for finite-frequency traveltimes - I. Theory," *Geophysical Journal International*, vol. 141, no. 1, pp. 157–174, 04 2000. [Online]. Available: https://dx.doi.org/10.1046/j.1365-246X.2000.00070.x

[32] W. Friederich, "The S-velocity structure of the East Asian mantle from inversion of shear and surface waveforms," *Geophysical Journal International*, vol. 153, pp. 88–102, 2003.

[33] K. Yoshizawa and B. L. N. Kennett, "Multi-mode surface wave tomography for the Australian region using a 3-stage approach incorporating finite-frequency effects," *Journal of Geophysical Research: Solid Earth*, vol. 109, p. doi:10.1029/2002JB002254, 2004.

[34] K. Sigloch, N. McQuarrie, and G. Nolet, "Two-stage subduction history under North America inferred from multiple-frequency tomography," *Nature Geoscience*, vol. 1, p. doi:10.1038/ngeo231, 2008.

[35] R. Montelli, G. Nolet, F. A. Dahlen, G. Masters, E. R. Engdahl, and S.-H. Hung, "Finite-frequency tomography reveals a variety of plumes in the mantle," *Science*, vol. 303, no. 5656, pp. 338–343, 2004. [Online]. Available: http://science.sciencemag.org/content/303/5656/338

[36] Y. Zhou, G. Nolet, F. A. Dahlen, and G. Laske, "Global upper-mantle structure from finite-frequency surface-wave tomography," *Journal of Geophysical Research: Solid Earth*, vol. 111, p. doi:10.1029/2005JB003677, 2006.

[37] E. D. Mercerat and G. Nolet, "On the linearity of cross-correlation delay times in finite-frequency tomography," *Geophysical Journal International*, vol. 192, no. 2, pp. 681–687, 12 2012. [Online]. Available: https://doi.org/10.1093/gji/ggs017

[38] A. M. Baig, F. A. Dahlen, and S.-H. Hung, "Traveltimes of waves in three-dimensional random media," *Geophysical Journal International*, vol. 153, no. 2, pp. 467–482, 05 2003. [Online]. Available: https://doi.org/10.1046/j.1365-246X.2003.01905.x

[39] J. Jocker, J. Spetzler, D. Smeulders, and J. Trampert, "Validation of first-order diffraction theory for the traveltimes and amplitudes of propagating waves," *Geophysics*, vol. 71, no. 6, pp. T167–T177, 2006. [Online]. Available: https://doi.org/10.1190/1.2358412

[40] A. Tarantola, "Theoretical background for the inversion of seismic waveforms, including elasticity and attenuation," *Pure and Applied Geophysics*, vol. 128, pp. 365–399, 1988.

[41] J. Tromp, C. Tape, and Q. Liu, "Seismic tomography, adjoint methods, time reversal and banana-doughnut kernels," *Geophysical Journal International*, vol. 160, no. 1, pp. 195–216, 01 2005. [Online]. Available: https://doi.org/10.1111/j.1365-246X.2004.02453.x

[42] A. Fichtner, H.-P. Bunge, and H. Igel, "The adjoint method in seismology - I. Theory," *Physics of the Earth and Planetary Interiors*, vol. 157, pp. 86–104, 2006.

[43] R.-E. Plessix, "A review of the adjoint-state method for computing the gradient of a functional with geophysical applications," *Geophysical Journal International*, vol. 167, pp. 495–503, 2006.

[44] A. Tarantola, "Linearized inversion of seismic reflection data," *Geophysical Prospecting*, vol. 32, no. 6, pp. 998–1015, 1984. [Online]. Available: https://onlinelibrary.wiley.com/doi/abs/10.1111/j.1365-2478.1984.tb00751.x

[45] G. Nolet, *A Breviary of Seismic Tomography: Imaging the Interior of the Earth and Sun*. Cambridge University Press, 2008.

[46] C. Li, G. S. Sandhu, O. Roy, N. Duric, V. Allada, and S. Schmidt, "Toward a practical ultrasound waveform tomography algorithm for improving breast imaging," *Proc. SPIE*, vol. 9040, 2014. [Online]. Available: https://doi.org/10.1117/12.2043686

[47] C. C. Paige and M. A. Saunders, "Lsqr: An algorithm for sparse linear equations and sparse least squares," *ACM Trans. Math. Softw.*, vol. 8, no. 1, pp. 43–71, Mar. 1982. [Online]. Available: http://doi.acm.org/10.1145/355984.355989

[48] J. Tong, F. A. Dahlen, G. Nolet, and H. Marquering, "Diffraction effects upon finite-frequency travel times: A simple 2-D example," *Geophysical Research Letters*, vol. 25, no. 11, pp. 1983–1986, 1998. [Online]. Available: https://agupubs.onlinelibrary.wiley.com/doi/abs/10.1029/98GL01291

[49] T. L. Jensen, J. H. Jørgensen, P. C. Hansen, and S. H. Jensen, "Implementation of an optimal first-order method for strongly convex total variation regularization," *BIT Numerical Mathematics*, vol. 52, no. 2, pp. 329–356, Jun 2012. [Online]. Available: https://doi.org/10.1007/s10543-011-0359-8

[50] A. Tarantola, *Inverse Problem Theory and Methods for Model Parameter Estimation*. Society for Industrial and Applied Mathematics, 2005. [Online]. Available: https://epubs.siam.org/doi/abs/10.1137/1.9780898717921

[51] H. Flath, L. Wilcox, V. Akçelik, J. Hill, B. van Bloemen Waanders, and O. Ghattas, "Fast algorithms for Bayesian uncertainty quantification in large-scale linear inverse problems based on low-rank partial hessian approximations," *SIAM Journal on Scientific Computing*, vol. 33, no. 1, pp. 407–432, 2011. [Online]. Available: https://doi.org/10.1137/090780717

[52] A. Fichtner and T. v. Leeuwen, "Resolution analysis by random probing," *Journal of Geophysical Research: Solid Earth*, vol. 120, no. 8, pp. 5549–5573, 2015. [Online]. Available: https://agupubs.onlinelibrary.wiley.com/doi/abs/10.1002/2015JB012106

[53] N. V. Ruiter, M. Zapf, T. Hopp, H. Gemmeke, K. W. A. van Dongen, J. Camacho, J. L. Herraiz, M. P. Liva, and J. M. Udías, "USCT reference data base: conclusions from the first SPIE USCT data challenge and future directions," *Proc. SPIE*, vol. 10580, p. 105800Q, 2018. [Online]. Available: https://doi.org/10.1117/12.2293063

[54] J. Camacho, L. Medina, J. F. Cruza, J. M. Moreno, and C. Fritsch, "Multimodal ultrasonic imaging for breast cancer detection," *Archives of Acoustics*, vol. 37, no. 3, pp. 253 – 260, 2012. [Online]. Available: https://content.sciendo.com/view/journals/aoa/37/3/article-p253.xml

[55] H. Gemmeke, R. Dapp, T. Hopp, M. Zapf, and N. V. Ruiter, "An improved 3D Ultrasound Computer Tomography system," in *2014 IEEE International Ultrasonics Symposium*, Sept 2014, pp. 1009–1012.

[56] N. Korta Martiartu, C. Boehm, N. Vinard, I. Jovanović Balic, and A. Fichtner, "Optimal experimental design to position transducers in ultrasound breast imaging," *Proc. SPIE*, vol. 10139, p. 101390M, 2017. [Online]. Available: https://doi.org/10.1117/12.2252514

[57] N. Korta Martiartu, C. Boehm, V. Hapla, H. Maurer, I. J. Balic, and A. Fichtner, "Optimal experimental design for joint reflection-transmission ultrasound breast imaging: From ray- to wave-based methods," *The Journal of the Acoustical Society of America*, vol. 146, no. 2, pp. 1252–1264, 2019. [Online]. Available: https://doi.org/10.1121/1.5122291

[58] A. Fichtner and J. Trampert, "Resolution analysis in full waveform inversion," *Geophysical Journal International*, vol. 187, no. 3, pp. 1604–1624, 2011. [Online]. Available: https://onlinelibrary.wiley.com/doi/abs/10.1111/j.1365-246X.2011.05218.x

[59] N. Duric, P. Littrup, A. Babkin, D. Chambers, S. Azevedo, A. Kalinin, R. Pevzner, M. Tokarev, E. Holsapple, O. Rama, and R. Duncan, "Development of ultrasound tomography for breast imaging: Technical assessment," *Medical Physics*, vol. 32, no. 5, pp. 1375–1386, 2005. [Online]. Available: https://aapm.onlinelibrary.wiley.com/doi/abs/10.1118/1.1897463

[60] H. M. Iyer and K. Hirahara, *Seiemic tomography, Theory and Practice*. Chapman & Hall, 1993.

Naiara Korta Martiartu has recently obtained her PhD in the Department of Earth Sciences at ETH Zurich. Her research has been focused on transferring knowledge from seismology to ultrasound breast imaging. She obtained her Bachelor in Physics from the University of Basque Country (UPV/EHU) and a Master in Geophysics from the University of Barcelona (UB). Furthermore, she has worked as research assistant at the Institute of Marine Sciences (Spanish National Research Council, CSIC) on full waveform inversion for acoustic-elastic scenarios. Her current research interests also include optimal experimental design problems, uncertainty quantification, and feminist and postcolonialist studies.

Christian Boehm is a senior researcher in the Department of Earth Sciences at ETH Zurich. He obtained his PhD in Mathematics from the Technical University of Munich in 2015. Furthermore, he holds a Master's degree in Mathematics and a joint Honours Degree in Technology Management from Technical University of Munich and Ludwig Maximilian University. He is a Co-Founder of Mondaic, an ETH spin-off that develops high performance software for full-waveform modelling and inversion. His research focuses on wave-based imaging, PDE-constrained optimization, and high-performance computing with applications in seismic tomography, medical imaging, and non-destructive testing.

Andreas Fichtner is Professor of Seismology and Wave Physics in the Department of Earth Sciences at ETH Zurich. His research is focused on the development of waveform inversion techniques, including a diverse range of aspects, such as numerical wave propagation through complex media, high-performance computing, large-scale data analysis, Bayesian inference and Monte Carlo methods, as well as effective medium theory. Though most applications are in seismic imaging for deep Earth structure, his group actively engages in technology transfer to medical imaging and material testing. Andreas is the author of 3 books on applied mathematics and geophysics, and of around 80 research papers in various international journals. He received early career awards from the American Geophysical Union and from the International Union of Geodesy and Geophyics. In addition to ETH Zurich, he has been affiliated with LMU Munich, Utrecht University, Stanford University and the Australian National University.